HHS Public Access

Author manuscript

Neuroimage. Author manuscript; available in PMC 2021 August 01.

Published in final edited form as:

Neuroimage. 2021 August 01; 236: 118071. doi:10.1016/j.neuroimage.2021.118071.

Early detection of Alzheimer's disease using creatine chemical exchange saturation transfer magnetic resonance imaging

Lin Chen[a,b,c], **Peter C.M. van Zijl**[a,b], **Zhiliang Wei**[a,b], **Hanzhang Lu**[a,b], **Wenzhen Duan**[d], **Philip C. Wong**[e,f], **Tong Li**[e,*], **Jiadi Xu**[a,b,*]

[a]F.M. Kirby Research Center for Functional Brain Imaging, Kennedy Krieger Research Institute, Baltimore, MD, USA

[b]Russell H. Morgan Department of Radiology and Radiological Science, The Johns Hopkins University School of Medicine, Baltimore, MD, USA

[c]Department of Electronic Science, Fujian Provincial Key Laboratory of Plasma and Magnetic Resonance, School of Electronic Science and Engineering, National Model Microelectronics College, Xiamen University, Xiamen, China

[d]Division of Neurobiology, Department of Psychiatry and Behavioral Sciences, Johns Hopkins University School of Medicine, Baltimore, MD 21205, USA

[e]Department of Pathology, The Johns Hopkins University School of Medicine, Baltimore, MD, USA

[f]Department of Neuroscience, The Johns Hopkins University School of Medicine, Baltimore, MD, USA

Abstract

Detecting Alzheimer's disease (AD) at an early stage brings a lot of benefits including disease management and actions to slow the progression of the disease. Here, we demonstrate that reduced creatine chemical exchange saturation transfer (CrCEST) contrast has the potential to serve as a new biomarker for early detection of AD. The results on wild type (WT) mice and two age-matched AD models, namely tauopathy (Tau) and Aβ amyloidosis (APP), indicated that CrCEST contrasts of the cortex and corpus callosum in the APP and Tau mice were significantly reduced compared to WT counterpart at an early stage (6-7 months) ($p < 0.011$). Two main causes of the reduced CrCEST contrast, i.e. cerebral pH and creatine concentration, were investigated. From phantom and hypercapnia experiments, CrCEST showed excellent sensitivity to pH variations. From MRS results, the creatine concentration in WT and AD mouse brain was equivalent, which suggests that the reduced CrCEST contrast was dominated by cerebral pH change involved in the

*Corresponding authors. xuj@kennedykrieger.org (J. Xu).

Author Contributions

Lin Chen and Jiadi Xu designed and performed experiments, processed data and wrote the manuscript; Peter van Zijl helped with interpreting the data and manuscript editing; Zhiliang Wei and Hanzhang Lu helped with the CO2 inhalation experiments; Philip Wong and Tong Li provided the animal models and performed the pathology experiments and analysis. Wenzhen Duan helped with the pathology analysis.

Supplementary materials

Supplementary material associated with this article can be found, in the online version, at doi:10.1016/j.neuroimage.2021.118071.

progression of AD. Immunohistochemical analysis revealed that the abnormal cerebral pH in AD mice may relate to neuroinflammation, a known factor that can cause pH reduction.

1. Introduction

Alzheimer's disease (AD) is the most common form of dementia and affects patients' daily life in many ways, such as speaking, impairments in memory, changes in mood and personality, problem-solving and other basic life skills (Huang and Mucke, 2012). Early diagnosis of AD would allow earlier treatment of people at risk, which will likely improve the performance of clinical trials. Many non-invasive biomarkers have been investigated for detecting AD, such as (i) the accumulation of neuritic plaques, which consist of an amyloid-beta (Aβ) core (Hardy and Selkoe, 2002; Selkoe and Kopan, 2003) and neurofibrillary tangles (NFT) that are composed of hyperphosphorylated tau (Ballatore et al., 2007; Lee and Trojanowski, 1999; Rojas and Boxer, 2016) in brain detected by positron emission tomography (PET) imaging (Saint-Aubert et al., 2017); (ii) levels of Aβ and tau in cerebrospinal fluid (CSF) (Barthelemy et al., 2020; Paterson et al., 2019); (iii) reduced glucose metabolism measured by 2-deoxy-2-(^{18}F) fluoro-D-glucose (^{18}FDG) PET (Mosconi et al., 2009) or MRI (Chen et al., 2021; Huang et al., 2020); (iv) brain atrophy revealed by structural imaging using MRI and CT (Frisoni et al., 2010). Despite the great detection sensitivity of PET imaging, the high cost and the use of radioactive tracers hinder its wide clinical application. Furthermore, the amyloid deposition detected by PET imaging can also occur in healthy aging, leading to falsely positive scan results. Brain atrophy revealed by structural imaging is a simple and less expensive alternative, but remains challenging to detect AD at the early stage since brain atrophy occurs at later stages of AD. Therefore, developing a cost-effective and widely available biomarker for early detection of AD has long been desired by patients, physicians, and scientists.

Chemical exchange saturation transfer (CEST) MRI is a versatile technique that can achieve enhanced sensitivity and spatial resolution on the standard clinical scanner by exploiting the exchange of protons between water and protein/metabolites (Jones et al., 2017; Kogan et al., 2013; van Zijl and Yadav, 2011; Vinogradov et al., 2013; Zhou and van Zijl, 2006). Recently, CEST was used for measuring the protein aggregation involved in AD on both animal models (Chen et al., 2018; Wang et al., 2019) and human patients (Zhang et al., 2020). In this study, we aimed to investigate the feasibility of the creatine chemical exchange saturation transfer (CrCEST) MRI in detecting AD at an early stage.

The creatine kinase reaction (CKR) plays a crucial role in energy transfer, and the PCr/Cr balance can provide valuable information on AD pathology (Burklen et al., 2006). In AD, CKR was found to decrease by as much as 86% (Pettegrew et al., 1994). To date, phosphorus-31 magnetic resonance spectroscopy (^{31}P MRS) has been the established method for non-invasively detecting the in vivo CKR function (Arnold et al., 1984; Hoult et al., 1974; Kemp and Radda, 1994). However, the inherently low detection sensitivity of ^{31}P MRS results in low spatial resolution and long acquisition times that hinder its wide application. In addition, ^{31}P MRS is not available on most magnetic resonance imaging (MRI) scanners in clinical practice due to additional hardware costs associated with ^{31}P

excitation/detection that are not used in clinical ^{1}H MRI scanners. On the other hand, CrCEST MRI not only provides high-resolution Cr mapping (Chen et al., 2020a; Goerke et al., 2014; Haris et al., 2012; Kogan et al., 2014), but also does not require special system hardware or coils and thus can be performed on standard clinical MRI scanners.

CrCEST contrast is sensitive to both the concentration of exchangeable protons and pH, the latter since the exchange rate of creatine guanidinium protons is strongly pH-dependent (Chen et al., 2020a; Goerke et al., 2014; Haris et al., 2012; Kogan et al., 2014). Cerebral pH regulation is crucial for cell functioning, enzyme activity and protein folding and pH status provides information that pertains to cell viability and neuronal degeneration (Chesler, 2003). Previous studies reveal that abnormal cerebral pH has an important role in the aggregation of Alzheimer-associated proteins (Atwood et al., 1998; Barrow and Zagorski, 1991; Burdick et al., 1992). Some studies also indicate that the reduced intracellular cerebral pH is a consequence of neuroinflammation involved in the development of AD (Fang et al., 2010; Morales et al., 2014; Schwartz et al., 2020). Hence, noninvasive *in vivo* assessment of cerebral pH could be a useful biomarker for the differentiation between early AD and healthy controls (Gonzales and Sumien, 2017; Lyros et al., 2020; Mandal et al., 2012). Currently, ^{31}P MRS (Jensen et al., 1988; Nishimura et al., 1989; Petroff et al., 1985) or ^{1}H MRS after administration of agents (Coman et al., 2020; Gil et al., 1992; Lyros et al., 2020; Vermathen et al., 2000) are well-established methods for detecting pH changes in tissue. However, MRS-based methods suffer from low detection sensitivity and a consequently low spatial resolution. Here, we applied CrCEST that includes information of the Cr/PCr balance and the cerebral pH changes in two AD mouse models, the amyloid precursor protein/presenilin-1 (APP) model (Drummond and Wisniewski, 2017) and the tau mouse model (Tau4RΔK) (Li et al., 2016). The feasibility to differentiate AD and wild type (WT) mice based on CrCEST was investigated. The two major contributions to the CrCEST signal variation, i.e. concentration and pH, were examined with the MRS based methods and hypercapnia experiments, respectively.

2. Materials and methods

2.1. Phantom preparation

The pH dependence of CrCEST signal was calibrated using two sets of phantoms. One set of phantoms consists of four Cr (50 mM) solutions mixed with 15% cross-linked BSA (CrossBSA). Here, CrossBSA was utilized to mimic the strong background signal present *in vivo*. BSA crosslinking was achieved using a 25 μL/mL glutaraldehyde solution. Another set of phantoms consists of four Cr (10 mM) solutions without CrossBSA. Phantoms were prepared in phosphate-buffered saline (PBS) and titrated to pH 6.4, 6.8, 7.2 and 7.6, respectively. One additional 15% CrossBSA phantom without Cr (pH 7.2) was prepared to validate the PLOF background fitting method. All phantoms were studied in 5 mm NMR tubes and maintained at 37 °C during MRI experiments by an air heater.

2.2. Ethics statement

All animal experiments were performed under the protocols based on the NIH Guidelines for Care and Use of Laboratory Animals. All experiments were performed in accordance

with the ARRIVE (Animal Research Reporting In Vivo Experiments) guidelines (Kilkenny et al., 2010), and approved by the Johns Hopkins University animal care and use committee.

2.3. Animal preparation

Five female mice (C57BL/6J) with an age of 6-7 months were employed for the optimization and comparison of the CEST contrasts. Thirty female mice with an age of 6–7 months were employed for the AD study, of which ten were Tau4RΔK (Tau) (Li et al., 2016), ten APP^{swe}:PS1ΔE9 (APP), and another ten are age-matched C57BL/6J (WT). Seven mice in each group were used for MRI, while three mice were sacrificed for immunohistochemical analysis. The Tau and APP transgenic mice were bred at Johns Hopkins University, according to details in the literature (Li et al., 2016). The onset of the tau tangles in the Tau mice typically starts at approximately six months. The APP transgenic mice co-expressed the Swedish variant of the amyloid precursor protein and the exon-9 deleted variant of presenilin1. The onset of neurotic plaques in biogenic APP mice typically starts at four to six months of age (Li et al., 2016). All mice were maintained under a 12L:12D cycle in a centralized animal housing facility program managed by Research Animal Resources (RAR) at Johns Hopkins University.

Hypercapnia will cause a reduction in cerebral intracellular pH (Martoft et al., 2003). To evaluate the sensitivity of CrCEST in detecting pH changes, Z-spectra were recorded on five WT mouse brains before and during 20% CO_2 inhalation, and the results compared with those obtained by amide proton transfer CEST (APT or amideCEST) MRI (Zhou et al., 2003), which is a classical CEST pH mapping method. The 20% CO_2 delivery was accomplished by mixing the air and pure CO_2 with flow rates of 2 L/min and 0.5 L/min, respectively. During the CO_2 inhalation, end-tidal CO_2 ($ETCO_2$) was measured constantly with a capnography monitor (Philips, Respironics NM3) in the mouse anesthesia nose cone. With a 20% CO_2 flow, the $ETCO_2$ is maintained at 90 ± 5 mmHg. To assure physiological stability, the during-CO_2 inhalation experiments were started 5 min after CO_2 delivery and took around 24 min.

2.4. MRI Experiments

All MRI experiments were performed on a horizontal bore 11.7 T Bruker Biospec system (Bruker, Ettlingen, Germany) equipped with actively shielded gradients with a maximum strength of 74 Gauss/cm. A 72 mm quadrature volume resonator was utilized for transmitting, and a 2 × 2 mouse phased array coil for detection. A double-tuned $^{31}P/^{1}H$ coil was employed for the collection of *in vivo* ^{31}P MRS. All coils were provided by Bruker. Anesthesia was induced using 2% isoflurane in medical air, followed by 1% to 1.5% isoflurane for maintenance during the MRI scan. The mouse head was positioned using a bite bar and two ear pins. During the MRI scan, mice were placed on a water-heated animal bed that was equipped with temperature and respiratory controls. The respiratory rate was monitored via a pressure sensor (SAII, Stony Brook, NY, USA) and maintained at 80-90 breaths per minute. The B_0 field over the mouse brain was adjusted using field mapping and second-order shimming.

All CEST experiments were performed using continuous-wave CEST (cwCEST). MR images were acquired using a Turbo Spin Echo (TSE) sequence with TE = 18 ms, TR = 5 s, TSE factor = 20, a matrix size of 64 × 64. For phantom experiments, the slice thickness was 2 mm and the field of view (FOV) was 15 × 15 mm^2. For animal experiments, the slice thickness was 1.5 mm and the FOV was 16 × 16 mm^2. The saturation field strength (B_1) and length for CrCEST were 2 μT and 1 s, respectively, according to previous studies (Chen et al., 2019b). The optimum saturation length was determined by the water rotating frame relaxation time and was found to be 2–3 s with 1 μT power and 1s with 2 μT power for CrCEST (Chen et al., 2019b). The optimum saturation power was found to be around 1 μT for amideCEST (Jin et al., 2013). As the acquisition parameters are similar for the two CEST contrasts, a saturation length of 2 s was implemented for the amideCEST. The frequency range measured to assess CrCEST was 1 to 3.5 ppm with an increment of 0.05 ppm, and the one for amideCEST was 2.3 ppm to 5 ppm with an increment of 0.1 ppm. S0 images for the CEST studies were acquired by setting the offset at 200 ppm. For the set of phantoms without CrossBSA, the saturation frequency was swept from −4 to 4 ppm with an increment of 0.2 ppm. A T_1 map was acquired using the RAREVTR sequence (RARE with variable TR = 0.5, 1, 1.5, 2, 3.5, 5, and 8 s) and a T_2 map was obtained using multi-slice multi-echo (MSME) MRI with geometry identical to that of the T_1 map and an echo spacing of 10 ms. The image slice was parallel to the coil and set to approximately −1.4 mm with respect to the anterior commissure (AC).

^{31}P MRS was performed to measure the cerebral pH change after CO_2 inhalation. The intracellular pH was calculated from the chemical shift of the Pi peak relative to the PCr peak (δ_{pi}) as follows (Petroff et al., 1985):

$$pH = 6.66 + \log(\delta - 3.08) / (5 / 57 - \delta) \quad (1)$$

In vivo ^{31}P MRS experiments were performed using a single BIR-4 adiabatic pulse with a 2 ms pulse width (TR = 2 s, NA = 512, bandwidth = 50 ppm, acquisition time = 100 ms). The total experimental time was 16 min. The coil was positioned above the center of the mouse brain, and the carrier frequency was set to the offset of the phosphocreatine (PCr) peak. All ^{31}P MRS were aligned by setting PCr peak as 0 ppm. One ^{31}P spectrum was collected as baseline, and another one five minutes after the start of CO_2 inhalation.

2.5. CEST data analysis

All CEST MRI images were processed using custom-written MATLAB scripts (MathWorks, www.mathworks.com, version 9.8.0.1417392 (R2020a) Update 4). The extraction and quantification of the CEST signal were achieved using polynomial and Lorentzian line-shape fitting (PLOF) as detailed previously (code available at https://github.com/LinChenMRI/PLOF.git) (Chen et al., 2019a; Chen et al., 2020a; Chen et al., 2020b; Chen et al., 2017). Briefly, the normalized steady-state Z-spectral intensity Z^{ss} can be converted to the longitudinal relaxation rate in the rotating frame, $R_{1\rho}$, e.g. the rotating-frame relaxation spectrum (R-spectrum) (Jin et al., 2011; Trott and Palmer, 2002; Zaiss and Bachert, 2013a; Zaiss and Bachert, 2013b). Asymmetry analysis, i.e. subtracting the label and control images acquired at two symmetric offsets with respect to water resonance, is the most commonly

used method to quantify CEST signal. This method was used for the quantitation of the CrCEST signal of the Cr solutions without CrossBSA, i.e. Z(−2 ppm) - Z(2 ppm). However, tissue contains many types of exchangeable protons on both sides of water in the Z-spectrum, such as the amine protons from proteins and glutamate at 2.5 ppm, the hydroxyl groups from proteins and Myo-inositol around 1 ppm, the relayed nuclear Overhauser effect (rNOE) CEST signals from choline at −1.6 ppm, and from the aliphatic protons in proteins and lipids between −4 and 0 ppm, making asymmetry analysis vulnerable to contaminations from lipids, proteins, semisolid macromolecules and other metabolites. The advantages of using the R-spectrum are that the rotating frame relaxation rate is linearly dependent on the concentration of the exchanging protons and that the rotating frame relaxation rates can be easily superimposed on each other when multiple exchanging pools present. Both amideCEST and CrCEST peaks (R) in the R-spectrum can be represented by a Lorentzian function:

$$R = R_{exch}\frac{(w\ /\ 2)^2}{(w\ /\ 2)^2 + (\Delta - \Delta_{exch})^2} \tag{2}$$

where w is the peak full-width-at-half-maximum (FWHM) of the Lorentzian line-shape. Δ is the offset. Δ_{exch} is the chemical shift offset of the CEST peak relative to the water signal, i.e. 3.5 ppm for amideCEST and 1.95 ppm for CrCEST; R_{exch} is the intensity of the amideCEST (R_{amide}) or CrCEST (R_{Cr}) peaks in the R-spectrum. The broad background (R_{amide}) in the R-spectrum can be represented by a polynomial function:

$$R_{back} = \sum_{n\ =\ 1}^{M} C_n(\Delta - \Delta_{exch})^n \tag{3}$$

where C_n terms are the zero to M-order polynomial coefficients. In this study, M was set to three for amideCEST. For CrCEST study, the peak is much close to the water signal. In order to improve the fitting, an updated background function was introduced by including one Lorentzian function to account for the water direct saturation (DS) (Sui et al., 2021):

$$R_{back} = \frac{C_0(C_1\ /\ 2)^2}{(C_1\ /\ 2)^2 + \Delta\omega^2} + C_2 + C_3 \cdot \Delta\omega \tag{4}$$

where the polynomial function ($C_2 + C_3 \cdot \Delta\omega$) was implemented to fit the background, consisting of magnetization transfer contrast (MTC) and exchanging protons such as amines and hydroxyls. We found that a linear function was sufficient to fit this combined background line shape between 1–3.5 ppm. A higher-order polynomial function may be needed when fitting a wider range. For both CrCEST and amideCEST, the Z-spectral range between [$\delta_{ini} - 0.4$, $\delta_{ini} + 0.4$] (ppm) was excluded from the background fitting, where δ_{ini} stands for the frequency offset of corresponding CEST peak. Multilinear singular value decomposition (MLSVD) was applied to enhance the CEST signal-to-noise ratio (SNR) (Chen et al., 2020a).

A two-sample t-test was performed between the R_{Cr}, T_1 and T_2 values for the WT, APP and Tau mice groups using the MATLAB built-in function "*ttest2*". A paired-sample t-test was

performed for the comparison between pre and post CO_2 inhalation using the MATLAB built-in function "*ttest*". t-test was considered statistically significant for $p < 0.05$ and highly significant when $p < 0.001$.

2.6. Validation of Cr Concentration Difference for AD and WT Mice Using ^{31}P and ^{1}H MRS

CEST contrast is sensitive to both pH and metabolite concentration. To account for non-pH effects, the Cr concentration in AD and WT mice was measured using ^{31}P and ^{1}H MRS. The concentration of total Cr (tCr=Cr+PCr) was determined by ^{1}H MRS, which was performed with a voxel of $3 \times 3 \times 3$ mm^3 using a stimulated echo acquisition mode (STEAM) sequence (TE = 3 ms, TM = 10 ms, TR = 2.5 s, NA = 256) with outer volume suppression (OVS). The water signal was suppressed by the variable power RF pulses and optimized relaxation delays (VAPOR) method (Tkac et al., 1999). An unsuppressed water signal was acquired before each ^{1}H MRS experiment with the same parameters except that the number of averages was one. First- and second-order shims were adjusted for each VOI using a field-mapping method. Brain Cr concentrations measured by *in vivo* ^{1}H MRS spectra were estimated using LCModel analysis as detailed in previous work (Chen et al., 2019a). A calibration phantom with 20 mM Cr mixed with CrossBSA (20% w, pH=7.2) was used for the calibration of the MRS quantification. The PCr and ATP concentration ratios on mouse brain were determined using ^{31}P MRS with identical experimental parameters, as previously mentioned. The ATP concentrations were considered constant in brain. The PCr and ATP concentration ratios were determined from the peak areas extracted by fitting the PCr peak at 0 ppm as well as the two ATP peaks at −2.6 ppm and −7.6 ppm using Lorentzian functions.

2.7. Immunohistochemical analysis of brains

To determine possible causes for the reduced pH values in AD animals, we performed immunohistochemical analysis on WT, APP and Tau mouse brain ($n = 3$). Four types of immunostaining were performed with antibodies specific to human Aβ (6E10: 1:1,000; SIG-39300, Covance) to monitor plaque accumulation, as well as antibodies specific to endogenous phosphorylated S422 of tau (pS422: 1:2,000; 44764G, Invitrogen, Carlsbad, CA) for examining tangle formation. Neuroinflammation in the AD brain was examined by looking at reactive astrocytes and microglia using polyclonal antiserum against Glial Fibrillary Acidic Protein (GFAP: Z0334, Dako Cooperation, Carpinteria, CA) and Ionized calcium-Binding Adapter molecule 1 (IBA1: CP290, Biocare Medical, CA), respectively. The preparation of the Immunohistochemical analysis has been detailed previously (Li et al., 2016). Briefly, the primary antibody prepared in blocking buffer (10% normal goat serum in PBS with 0.3% Triton-X) was applied overnight at 4 °C, followed by a secondary antibody for 30 min incubation at room temperature. Sections for immunofluorescence were examined under a Zeiss LSM 510 laser scanning fluorescence confocal microscope. For the secondary antibody and avidin-biotinylated peroxidase system, we used the Vectastain Universal Elite ABC kit (Vector Laboratories). The proteins were visualized with DAB, and if required, slides were counterstain with Hematoxylin.

3. Results

3.1. Phantom validation of CrCEST in detecting pH change

The typical Z-spectrum ($Z = S/S_0$) of CrossBSA without Cr and its PLOF fitting are shown in Fig. 1a. It can be seen that the combined MTC and DS background is well represented by the background function in Eq. 4. The representative Z-spectrum of CrossBSA with 50 mM Cr is shown in Fig. 1b, where a well-defined CEST peak at 2 ppm is observed. These data show that PLOF is able to fit both the background and extract the CEST peak. The fitted CrCEST signal (ΔZ_{Cr}) and apparent relaxation rate (R_{Cr}) are plotted as a function of pH in Figs. 1c,d. From the results, the relationship between ΔZ_{Cr}, R_{Cr} and pH within the physiologically relevant range (6.4-7.6) can be described with the following linear functions:

$$\Delta Z_{Cr} = 0.18 \cdot pH - 1.10 \quad (5)$$

$$R_{Cr} = 0.06 \cdot pH - 0.34 \quad (6)$$

The typical Z-spectra of the Cr solutions without CrossBSA are plotted in Fig. 1e. The Cr peak coalesced with water when pH reached 7.6. The pH dependence of the CrCEST signal in the Cr solutions is shown in Fig. 1f. The CrCEST signal is inversely dependent on the pH values when pH value is larger than 6.8 with a saturation power of 2 μT and 1 s saturation length.

3.2. Validation of the use of CrCEST for detecting subtle cerebral pH changes

To validate the feasibility of CrCEST MRI in detecting subtle cerebral pH changes, Z-spectra were recorded of WT mouse brain before and during 20% CO_2 inhalation, as shown in Figs. 2c and 2d, respectively. AmideCEST MRI was also performed for comparison, as shown in Figs. 2a, b. The CEST signals ΔZ and corresponding apparent relaxation terms R extracted by PLOF are plotted in Figs. 2e,f. The ΔZ and R obtained by CrCEST before CO_2 inhalation were larger than those from amideCEST ΔZ_{Cr}: 2.91 ± 0.35%, ΔZ_{amide}: 1.87 ± 0.39%, $p < 0.01$; R_{Cr}: 0.103±0.014, R_{amide}: 0.023 ± 0.005, $p < 0.01$, $n = 5$). During CO_2 inhalation, CrCEST showed significantly reduced (ΔZ and $R\,\Delta Z_{Crdiff}$: 1.10 ± 0.47%, $p < 0.01$; R_{Crdiff}: 0.032 ± 0.015, $p = 0.016$), while no significant difference was observed in amideCEST ($\Delta Z_{amidediff}$: 0.64 ± 0.59%, $p = 0.075$; $R_{amidediff}$: 0.008 ± 0.007, $p = 0.069$). B_0 and B_1 maps on the mouse brain were measured and are shown in the Supplementary Materials Fig. S1. Both B_0 and B_1 were homogeneous across brain with standard deviations of around 0.09 ppm and 0.12, respectively.

^{31}P MRS was performed to quantify both the pH change and PCr concentration variation during CO_2 inhalation. The averaged ^{31}P MRS spectra ($n = 4$) collected before and during CO_2 inhalation are plotted in Fig. 2g. The ^{31}P coil coverage is illustrated by the T_2-weighted image shown in the inlet figure of Fig. 2g. The typical ^{31}P peaks in mouse brain, such as PCr, adenosine triphosphate (ATP), Pi, and lipids, can be well observed in the spectrum. The P_i peak shifted from 5.07 ± 0.06 ppm to 4.77 ± 0.08 ppm during CO_2 inhalation, which indicates a cerebral pH change from 7.26 ± 0.07 to 6.99 ± 0.07 according to Eq. 1. The PCr

peak broadened and also the concentration decreased by approximately 9.6 ± 5%, as determined from the integral (before: $2.18 \pm 1.1 \times 10^{4,}$ after: $1.97 \pm 1.0 \times 10^{4}$), which is caused by the conversion of PCr to Cr as pH decreases (Litt et al., 1985; Nishimura et al., 1989). With 20% CO_2 inhalation, the T_1 value of the cortex was reduced from 1.90 ± 0.07 s ($n = 5$) to 1.82 ± 0.07 s ($n = 5$), while the T_2 value changed from 37.9±0.7 ms ($n = 5$) to 37.3±1.2 ms ($n = 5$). To remove MTC and T_1-induced CEST signal changes, the apparent relaxation rate of Cr (R_{Cr}) was calculated according to Eqs. 2 and 4. The averaged R_{Cr} for the whole brain decreased from 0.103 ± 0.014 s^{-1} to 0.071 ± 0.019 s^{-1} after CO_2 inhalation, which gives the relation between the CrCEST variation (R_{Crdiff}) and the pH changes:

$$R_{Crdiff} = 0.12 \cdot \Delta pH \tag{7}$$

3.3. Differentiating AD and WT mice using CrCEST MRI

Typical CrCEST Z-spectra of the WT and AD cortex (red ROI) are plotted in Figs. 3 d-f together with the PLOF fitting curves. The MTC and other CEST background could be fitted well with Eq. 4. Due to the strong macromolecular background, a small change in B_1 value can introduce shifts in the Z-spectra between different mice. However, the Z-values at 1 and 3.5 ppm were similar for all mice and not correlated with the disease as demonstrated by the background values at both 1 and 3.5 ppm for the three groups of mice (supplemental Fig. S2). R_{Cr} maps of AD and WT mouse brain, together with corresponding S_0 images, T_1 maps, and T_2 maps, are shown in Fig. 3. Here, R_{Cr}, instead of ΔZ_{Cr}, was selected to represent CrCEST data because R_{Cr} can compensate for the scaled-down effect introduced by MTC or T_1 differences (Chen et al., 2019b). Compared to the WT results, reduced R_{Cr} intensities are observed for the Tau and APP mouse brains, especially in the cortical regions. The T_1 and T_2 maps were similar between different mice.

Extracted regional R_{Cr}, T_1 and T_2 values are summarized in Fig. 4 and Table 1. Three regions of interest (ROIs), namely cortex (cx), thalamus (th), and corpus callosum (cc), were chosen, as illustrated in Fig. 3a. Significant differences were obtained between WT and the APP R_{Cr} values for the cortex and corpus callosum. The APP R_{Cr} values of the thalamus were significantly lower than those for WT, while the Tau thalamus R_{Cr} values showed a nonsignificant trend to be lower than WT. No significant difference was observed for the regional T_1 values among the three types of mice. For all mouse types, the thalamic T_1 was smaller than that of the cortex ($p < 0.01$) (Table 1 and Fig. 4). The T_2 values were similar for WT, APP and Tau mice. Similar to the T_1 values, the thalamic T_2 values were smaller than those in the cortex for all mice ($p < 0.01$) (Table 1 and Fig. 4).

3.4. Cr concentration measured by ^{31}P and proton MRS

CEST contrast is sensitive to metabolite concentration and pH. To exclude potential contributions from concentration variations to the reduced CrCEST contrast observed in APP and Tau mouse brains, the PCr and total Cr (tCr = PCr + Cr) concentrations were measured using ^{31}P and ^{1}H MRS, respectively. Typical ^{1}H MRS brain spectra of WT, Tau and APP mice are plotted in Figs. 5-c, respectively. With a voxel size of 27 mm^3, high-resolution proton MR spectra were achieved on all mice. The tCr quantification results from

the LCModel are reported in Fig. 5d, showing no distinct difference between the three types of mice (WT: 6.5±0.9 mM; APP: 6.9±1.1 mM, $p = 0.6$; Tau: 6.8± 0.8 mM, $p = 0.7$). To examine the neuronal integrity, the NAA concentrations were also extracted and found to be 5.5 ± 0.8 (WT), 4.7±1.2 (APP) and 5.1 ± 1.0 (Tau), respectively. While the NAA concentrations of APP and Tau AD mice were slightly lower than those of WT mice, this difference was not significant (APP vs WT $p = 0.24$; Tau vs WT $p = 0.45$). The averaged ^{31}P spectra in Figs. 5e-g show similar PCr intensities for the three types of mice (WT: 1372±326; Tau: 1357±141, $p = 0.8$; APP: 1416±263, $p = 0.9$). The PCr intensities were scaled based on the averaged ATP peak intensities at −2.5 ppm and −7.7 ppm. The PCr concentration ratios with respect to ATP were extracted and did not significantly differ between the three types of mice (WT: 2.42±0.14; Tau: 2.45±0.34, $p = 0.9$; APP: 2.38±0.43, $p = 0.9$), which is consistent with the ^{31}P MRS observation in Figs. 5e-g. These ^{31}P and ^{1}H data show that the concentrations of PCr and Cr in AD and WT mouse brain were not significantly different. This result suggests that pH change is the dominant contribution to the reduced CEST contrast observed in AD mouse brains. The Pi chemical shifts in the averaged 31P MRS are 5.07 ppm (WT), 4.92 ppm (Tau) and 4.87 ppm (APP), respectively (Figs. 5e,f and g), which further confirms the pH reduction in the AD mice.

3.5. Immunohistochemical results of AD brains

Typical immunohistochemical analysis results for the cortex region of the WT, APP and Tau mouse brains are plotted in Fig. 6. At this age (e.g. 6–7 months), plaques were abundant in APP mice, while not yet detectable in Tau and WT mice (Fig. 6a). Tau tangles were still very rare at this age (Fig. 6b), which is consistent with a previous observation that widespread tangles occur after 9 months on mouse brain (Li et al., 2016). Hypertrophic GFAP positive astrocytes were observed in cortical regions of APP mice but not Tau mice (Fig. 6c). Similar to the astrocyte results, the IBA1 histological analysis confirmed activation of microglia in the APP mice, while weak microglial activation was observed in the Tau mice.

4. Discussion

In this study, we demonstrated that reduced CrCEST contrast has the potential to differentiate AD and WT mice at an early stage (6-7 months). CrCEST MRI can be performed on a standard MRI scanner without requirements for additional (heteronuclear) hardware or contrast agents, which is promising for widespread applications. From ^{1}H MRS and ^{31}P MRS results, Cr concentration did not show a significant difference between this group of AD and WT mice at an age of 6–7 months. Hence, the main factor that altered the CrCEST contrast in AD mice was attributed to cerebral pH change. From the calibration function in Eq. 7, the cortical pH reduced by about 0.26±0.07 in APP mice and about 0.18±0.16 in Tau mice.

Currently, due to the lack of sensitive and routine methods for non-invasively mapping pH *in vivo*, only limited studies have been performed to investigate pH effects in AD mouse brain (Lyros et al., 2020; Mandal et al., 2012; Rijpma et al., 2018). The pH detection sensitivity of CEST MRI is proportional to the change in the exchange rate change induced by pH

variations. Even though amideCEST MRI has been successful in measuring the large pH change in acute ischemia and other diseases (Chen et al., 2020a; Goerke et al., 2014; Haris et al., 2012; Kogan et al., 2014; Leigh et al., 2018), the slow exchange rate of amide protons (<400 Hz range) (Heo et al., 2019) at physiologically relevant temperature and pH limits its sensitivity in detecting subtle pH changes, as demonstrated in CO_2 inhalation experiments. Compared to amide protons, Cr guanidinium protons possess an exchange rate of around 1000 Hz (Goerke et al., 2014), resulting in a larger absolute exchange rate change with pH.

According to previous studies (Saab et al., 2002; Sugden and Fuller, 1991), Cr is located in the intracellular compartment, which suggests that the pH measurements obtained by CrCEST reflect mainly the intracellular environment, which is consistent with the measurements obtained by ^{31}P MRS (Gasparovic et al., 1998). Currently, there is no consensus on the cause of intracellular pH reduction in AD. Some studies imply that abnormal cerebral pH may arise from neuroinflammation and consequent changes in cellular metabolism (Eikelenboom et al., 2010; Fang et al., 2010; Jonsson et al., 2013; Mandal et al., 2012; Schwartz et al., 2020). In this study, the comparison between Tau mice and APP mice provides some indication of the cause of abnormal cerebral pH in AD. It is known that the pH in the mammalian central neural system is regulated by several types of acid transport mechanisms such as Na^+/H^+ pumps (Tse et al., 1993), Cl^-/HCO_3^- pumps (Thomas, 1976, 1977) and Na^+/HCO_3^- cotransporters (Boron and Boulpaep, 1983). The ability of the cell to regulate pH reflects the neuronal viability since the membrane Na^+/H^+ channel pumps require a continuous supply of ATP molecules to maintain cellular homeostasis. Minimal neuronal loss was observed in the APP mice even at the late stage of AD (>20 months), and no neuronal loss was observed in Tau mice at 6-7 months (Li et al., 2016). Hence, the significant pH reduction in the two mouse models at this early stage occurs before impaired neuronal function, which has been postulated to be a consequence of cellular apoptosis signaling due to intracellular pH decrease (Fang et al., 2010; Schwartz et al., 2020). On the other hand, inflammation is a well-established pathological feature in the brains of patients with Alzheimer's disease, as illustrated by an accumulation of activated microglia and astrocytes around both plaques and tau tangles (Jonsson et al., 2013; Maeda et al., 2011). Studies of P301S tau transgenic mice established that hippocampal synaptic pathology and microgliosis precede tau tangle formation and neurodegeneration (Maeda et al., 2011; Yoshiyama et al., 2007). The co-localization of neuroinflammation and Tau pathology was further confirmed in a recent study of frontotemporal dementia (Bevan-Jones et al., 2020). Presence of significant neuroinflammation in terms of activation of astrocytes/microglia in APP mice was confirmed by immunohistochemical analysis (Fig. 6). Recent direct evidence suggests that neuroinflammation can also contribute to the production of amyloid-β through an interferon-induced transmembrane protein 3 IFITM3–γ-secretase complex (Hur et al., 2020; Tomiyama et al., 2010). Hence, neuroinflammation could be a major cause of the intracellular pH reduction in both APP and Tau mice (Fang et al., 2010; Schwartz et al., 2020). In the current study, significant neuroinflammation was observed in the early stage of AD in APP mouse (Fig. 6c), which is consistent with another *in vivo* observation that inflammation is an early event in AD patients and can be detected in MCI subjects, even when amyloid deposition is not detectable (Eikelenboom et al., 2010). However, there was no clear neuroinflammation in Tau mice (Fig. 6d) at this stage, which suggests that factors in

addition to neuroinflammation contribute to the pH reduction, which needs further investigation. A previous ^{31}P MRS study on AD patients reported an elevated PCr concentration in AD (approximately 5% increment) (Rijpma et al., 2018), which may contribute to a small portion of the CrCEST reduction in this study, assuming that the tCr is constant. In our study, we did not observe significant PCr changes in the AD models.

Previous pathology studies on the APP and Tau animal models showed that the tangles and plaques just begin to appear at the age of 6-7 months (Li et al., 2016). Thus, the pH reduction appears to precede or coincide with this pathology and the CrCEST based pH mapping has potential as a non-invasive biomarker for early diagnosis of AD. This method also provides a sensitive pH mapping method for understanding the mechanisms that underlie AD and potentially for monitoring therapeutic outcomes. Compared to the commonly applied ^{31}P MRS, CEST MRI not only offers much higher detection sensitivity but also works on most MRI scanners in clinical practice without additional hardware costs.

A previous study demonstrated that protein aggregation has the potential to alter the background signal due to changes in amide and aromatic rNOE contributions. (Chen et al., 2018; Kleimaier et al., 2020) However, the protein aggregation in the APP mice is expected to be dominant at the late stage (>12 months) and protein aggregation has not been reported in Tau mice (Li et al., 2016). Therefore, the reduced CrCEST signal in both APP and Tau mice can not be explained by protein aggregation. The Z-values at both 1 and 3.5 ppm, which include the amide and aromatic rNOE values, showed similar values, as demonstrated in the supplemental Fig. S2. This further confirms that protein aggregation did not contribute to the observed CrCEST reduction in the AD mice at early stage.

In vivo tissue contains various exchangeable protons, and their CEST signals are modulated by the saturation parameters (van Zijl et al., 2018). In this study, a saturation pulse of 2 μT power and 1 s length was adopted. From the Cr phantom study, the Cr signal is positively dependent on the pH value when mixing with CrossBSA, which is consistent with the observation in the hypercapnia study on mouse brain (Fig. 2e) as well as the previous CrCEST study on the ischemic stroke animal model (Chen et al., 2020a). However, the CrCEST signal is inversely dependent on the pH in the Cr solutions (Fig. 1f) between the physiologically relevant pH range (6.8–7.2) In order to understand this pH dependence, we performed Bloch simulation by assuming three pools, i.e. water, creatine and macromolecular pool, and the simulation results were presented in the Supplementary Materials Fig. S3. From the simulation results (Fig. S3b), it suggested that the exchange rate of CrCEST in both CrossBSA and mouse brain is significantly slower than that in the Cr solutions, which has been observed previously (Zaiss et al., 2015). The exact exchange rate of Cr in brain still needs to be further validated, which is beyond the scope of the current study. According to our previous studies (Chen et al., 2019b; Chen et al., 2017) and work from another group (Zhang et al., 2017), the guanidinium (Guan) protons from arginine side chains in mobile proteins also contribute (less than 20%) to the CEST signal at 2 ppm with these saturation parameters. Lower saturation power and longer saturation length will lead to a larger contribution from Guan proton to CEST signal at 2 ppm. On contrary to CrCEST in brain, GuanCEST contrast shows an opposite trend regarding pH reduction, which means lower pH yields higher GuanCEST contrast as evidenced by both eggwhite phantom (Sui et

al., 2021) and ischemic stroke studies (Jin et al., 2017; Zhou et al., 2019). Therefore, in practice, appropriate saturation parameters should be chosen to ensure the CEST signal at 2 ppm is dominated by Cr. As demonstrated in the Bloch simulation (Fig. S3b), the CrCEST signal is dominant at high saturation powers (>2 μT) by assuming the Cr exchange rate in mouse brain is 500 Hz. It should be noticed that the saturation parameters used in this study were designed for high magnetic fields. However, the CEST contrast depends on field strength and while PCr has been detected at 3T, Cr is more difficult. Thus, further studies will have to prove the use of this approach in the clinic. The fitting method is also crucial for extracting accurate CEST contrast. In this study, we improved the polynomial function (Eq. 4) to fit the background from MTC and contributions from fast-exchanging protons, as demonstrated in Fig. 1a. Another benefit of the updated background function was excellent robustness against signal oscillation. From Figs. 3 d-f, the updated background function worked well even with obvious signal oscillation between 3.0 ppm to 3.5 ppm.

The current approach is ready to be transferred to high-field clinical scanners, such as 7T scanners. When the magnetic field is reduced to 3 T, the exchange rate of Cr can no longer be considered to be in the intermediate exchange regime. The guanidinium peak of Cr coalesces with the water peak because of the reduced shift difference at these lower fields and overlaps with many other exchanging protons. As a consequence, the separation of the Cr CEST signal will be very challenging. Fortunately, it was recently shown that the detection of PCr is feasible at 3T because of its much slower exchange rate (Chen et al., 2020b), which may serve as an appropriate alternative at lower magnetic field.

5. Conclusion

The feasibility of using CrCEST MRI to differentiate AD and WT mice at an early stage was demonstrated. The results indicate that AD mice (APP and Tau) at 6-7 months have reduced intracellular pH compared to age-matched WT mice, which preceded the tangle and plaque formation. This finding was tentatively attributed to the neuroinflammation of AD mice. The results suggest that reduced CrCEST contrast has the potential to serve as a new biomarker for detecting AD at an early stage.

Supplementary Material

Refer to Web version on PubMed Central for supplementary material.

Acknowledgments

Grant support from NIH: R01HL149742, R21NS118079, R21AG065794, P50AG05146, P41EB015909, R01EB015032, and DOD W81XWH-18-1-0797.

References

Arnold DL, Matthews PM, Radda GK, 1984. Metabolic recovery after exercise and the assessment of mitochondrial function in vivo in human skeletal muscle by means of 31P NMR. Magn. Reson. Med 1, 307–315. [PubMed: 6571561]

Atwood CS, Moir RD, Huang X, Scarpa RC, Bacarra NME, Romano DM, Hartshorn MA, Tanzi RE, Bush AI, 1998. Dramatic aggregation of Alzheimer Aβ by Cu (II) is induced by conditions representing physiological acidosis. J. Biol. Chem 273, 12817–12826. [PubMed: 9582309]

Ballatore C, Lee VM, Trojanowski JQ, 2007. Tau-mediated neurodegeneration in Alzheimer's disease and related disorders. Nat. Rev. Neurol 8, 663–672.

Barrow CJ, Zagorski MG, 1991. Solution structures of beta peptide and its constituent fragments: relation to amyloid deposition. Science 253, 179–182. [PubMed: 1853202]

Barthelemy NR, Li Y, Joseph-Mathurin N, Gordon BA, Hassenstab J, Benzinger TLS, Buckles V, Fagan AM, Perrin RJ, Goate AM, Morris JC, Karch CM, Xiong C, Allegri R, Mendez PC, Berman SB, Ikeuchi T, Mori H, Shimada H, Shoji M, Suzuki K, Noble J, Farlow M, Chhatwal J, Graff-Radford NR, Salloway S, Schofield PR, Masters CL, Martins RN, O'Connor A, Fox NC, Levin J, Jucker M, Gabelle A, Lehmann S, Sato C, Bateman RJ, McDade E, Dominantly Inherited Alzheimer, N. 2020. A soluble phosphorylated tau signature links tau, amyloid and the evolution of stages of dominantly inherited Alzheimer's disease. Nat. Med 26, 398–407. [PubMed: 32161412]

Bevan-Jones WR, Cope TE, Jones PS, Kaalund SS, Passamonti L, Allinson K, Green O, Hong YT, Fryer TD, Arnold R, Coles JP, Aigbirhio FI, Larner AJ, Patterson K, O'Brien JT, Rowe JB, 2020. Neuroinflammation and protein aggregation co-localize across the frontotemporal dementia spectrum. Brain 143, 1010–1026. [PubMed: 32179883]

Boron WF, Boulpaep EL, 1983. Intracellular pH regulation in the renal proximal tubule of the salamander. Na-H exchange. J Gen Physiol 81, 29–52. [PubMed: 6833996]

Burdick D, Soreghan B, Kwon M, Kosmoski J, Knauer M, Henschen A, Yates J, Cotman C, Glabe C, 1992. Assembly and aggregation properties of synthetic Alzheimer's A4/beta amyloid peptide analogs. J. Biol. Chem 267, 546–554. [PubMed: 1730616]

Burklen TS, Schlattner U, Homayouni R, Gough K, Rak M, Szeghalmi A, Wallimann T, 2006. The creatine kinase/creatine connection to Alzheimer's disease: CK--inactivation, APP-CK complexes and focal creatine deposits. J Biomed Biotechnol 35936 2006. [PubMed: 17047305]

Chen L, Barker PB, Weiss RG, van Zijl PCM, Xu J, 2019a. Creatine and phosphocreatine mapping of mouse skeletal muscle by a polynomial and Lorentzian line-shape fitting CEST method. Magn. Reson. Med 81, 69–78. [PubMed: 30246265]

Chen L, Cao S, Koehler RC, van Zijl PCM, Xu J, 2020a. High-sensitivity CEST mapping using a spatiotemporal correlation-enhanced method. Magn Reson Med doi:10.1002/mrm.28380.

Chen L, Schar M, Chan KWY, Huang J, Wei Z, Lu H, Qin Q, Weiss RG, van Zijl PCM, Xu J, 2020b. In vivo imaging of phosphocreatine with artificial neural networks. Nat. Commun 11, 1072. [PubMed: 32102999]

Chen L, Wei Z, Cai S, Li Y, Liu G, Lu H, Weiss RG, van Zijl PCM, Xu J, 2019b. High-resolution creatine mapping of mouse brain at 11.7 T using non-steady-state chemical exchange saturation transfer. NMR Biomed 32 e4168. [PubMed: 31461196]

Chen L, Wei Z, Chan KW, Li Y, Suchal K, Bi S, Huang J, Xu X, Wong PC, Lu H, van Zijl PC, Li T, Xu J, 2021. D-Glucose uptake and clearance in the tauopathy Alzheimer's disease mouse brain detected by on-resonance variable delay multiple pulse MRI. J. Cereb. Blood Flow Metab 41 (5), 1013–1025. [PubMed: 32669023]

Chen L, Wei Z, Chan KWY, Cai S, Liu G, Lu H, Wong PC, van Zijl PCM, Li T, Xu J, 2018. Protein aggregation linked to Alzheimer's disease revealed by saturation transfer MRI. Neuroimage 188, 380–390. [PubMed: 30553917]

Chen L, Zeng H, Xu X, Yadav NN, Cai S, Puts NA, Barker PB, Li T, Weiss RG, van Zijl PCM, Xu J, 2017. Investigation of the contribution of total creatine to the CEST Z-spectrum of brain using a knockout mouse model. NMR Biomed 30, e3834.

Chesler M, 2003. Regulation and modulation of pH in the brain. Physiol. Rev 83, 1183–1221. [PubMed: 14506304]

Coman D, Peters DC, Walsh JJ, Savic LJ, Huber S, Sinusas AJ, Lin M, Chapiro J, Constable RT, Rothman DL, Duncan JS, Hyder F, 2020. Extracellular pH mapping of liver cancer on a clinical 3T MRI scanner. Magn Reson Med 83, 1553–1564. [PubMed: 31691371]

Drummond E, Wisniewski T, 2017. Alzheimer's disease: experimental models and reality. Acta Neuropathol 133, 155–175. [PubMed: 28025715]

Eikelenboom P, van Exel E, Hoozemans JJ, Veerhuis R, Rozemuller AJ, van Gool WA, 2010. Neuroinflammation - an early event in both the history and pathogenesis of Alzheimer's disease. Neurodegener Dis 7, 38–41. [PubMed: 20160456]

Fang B, Wang D, Huang M, Yu G, Li H, 2010. Hypothesis on the relationship between the change in intracellular pH and incidence of sporadic Alzheimer's disease or vascular dementia. Int J Neurosci 120, 591–595. [PubMed: 20707633]

Frisoni GB, Fox NC, Jack CR Jr., Scheltens P, Thompson PM, 2010. The clinical use of structural MRI in Alzheimer disease. Nat Rev Neurol 6, 67–77. [PubMed: 20139996]

Gasparovic C, Barba I, Born J, Barton S, Arus C, Mann P, 1998. A study of imidazole-based nuclear magnetic resonance probes of cellular pH. Anal Biochem 261, 64–72. [PubMed: 9683513]

Gil MS, Cruz F, Cerdán S, Ballesteros P, 1992. Imidazol-1-ylalkanoate esters and their corresponding acids. A novel series of extrinsic 1H NMR probes for intracellular pH. Bioorg. Med. Chem. Lett 2, 1717–1722.

Goerke S, Zaiss M, Bachert P, 2014. Characterization of creatine guanidinium proton exchange by water-exchange (WEX) spectroscopy for absolute-pH CEST imaging in vitro. NMR Biomed 27, 507–518. [PubMed: 24535718]

Gonzales EB, Sumien N, 2017. Acidity and Acid-sensing ion channels in the normal and Alzheimer's disease brain. J. Alzheimers Dis 57, 1137–1144. [PubMed: 28211811]

Hardy J, Selkoe DJ, 2002. The amyloid hypothesis of Alzheimer's disease: progress and problems on the road to therapeutics. Science 297, 353–356. [PubMed: 12130773]

Haris M, Nanga RP, Singh A, Cai K, Kogan F, Hariharan H, Reddy R, 2012. Exchange rates of creatine kinase metabolites: feasibility of imaging creatine by chemical exchange saturation transfer MRI. NMR Biomed. 25, 1305–1309. [PubMed: 22431193]

Heo HY, Han Z, Jiang S, Schar M, Zhou J, 2019. Quantifying amide proton exchange rate and concentration in chemical exchange saturation transfer imaging of the human brain. Neuroimage 189, 202–213. [PubMed: 30654175]

Hoult DI, Busby SJ, Gadian DG, Radda GK, Richards RE, Seeley PJ, 1974. Observation of tissue metabolites using 31P nuclear magnetic resonance. Nature 252, 285–287. [PubMed: 4431445]

Huang J, van Zijl PCM, Han X, Dong CM, Cheng GWY, Tse KH, Knutsson L, Chen L, Lai JHC, Wu EX, Xu J, Chan KWY, 2020. Altered d-glucose in brain parenchyma and cerebrospinal fluid of early Alzheimer's disease detected by dynamic glucose-enhanced MRI. Sci. Adv 6 eaba3884. [PubMed: 32426510]

Huang Y, Mucke L, 2012. Alzheimer mechanisms and therapeutic strategies. Cell 148, 1204–1222. [PubMed: 22424230]

Hur JY, Frost GR, Wu X, Crump C, Pan SJ, Wong E, Barros M, Li T, Nie P, Zhai Y, Wang JC, Tcw J, Guo L, McKenzie A, Ming C, Zhou X, Wang M, Sagi Y, Renton AE, Esposito BT, Kim Y, Sadleir KR, Trinh I, Rissman RA, Vassar R, Zhang B, Johnson DS, Masliah E, Greengard P, Goate A, Li YM, 2020. The innate immunity protein IFITM3 modulates gamma-secretase in Alzheimer's disease. Nature, 10.1038/s41586-41020-42681-41582.

Jensen KE, Thomsen C, Henriksen O, 1988. vivo measurement of intracellular pH in human brain during different tensions of carbon dioxide in arterial blood. A 31P-NMR study. Acta Physiol. Scand 134 295–292, g298. [PubMed: 3147578]

Jin T, Autio J, Obata T, Kim SG, 2011. Spin-locking versus chemical exchange saturation transfer MRI for investigating chemical exchange process between water and labile metabolite protons. Magn. Reson. Med 65, 1448–1460. [PubMed: 21500270]

Jin T, Wang P, Hitchens TK, Kim SG, 2017. Enhancing sensitivity of pH-weighted MRI with combination of amide and guanidyl CEST. Neuroimage 157, 341–350. [PubMed: 28602944]

Jin T, Wang P, Zong X, Kim S-G, 2013. MR imaging of the amide-proton transfer effect and the pH-insensitive nuclear overhauser effect at 9.4 T. Magn. Reson. Med 69, 760–770. [PubMed: 22577042]

Jones KM, Pollard AC, Pagel MD, 2017. Clinical applications of chemical exchange saturation transfer (CEST) MRI. J. Magn. Reson. Imaging doi:10.1002/jmri.25838.

Jonsson T, Stefansson H, Steinberg S, Jonsdottir I, Jonsson PV, Snaedal J, Bjornsson S, Huttenlocher J, Levey AI, Lah JJ, Rujescu D, Hampel H, Giegling I, Andreassen OA, Engedal K, Ulstein I, Djurovic S, Ibrahim-Verbaas C, Hofman A, Ikram MA, van Duijn CM, Thorsteinsdottir U, Kong A, Stefansson K, 2013 Variant of TREM2 associated with the risk of Alzheimer's disease. N. Eng. J. Med 368, 107–116.

Kemp GJ, Radda GK, 1994. Quantitative interpretation of bioenergetic data from 31P and 1H magnetic resonance spectroscopic studies of skeletal muscle: an analytical review. Magn. Reson Q 10, 43–63. [PubMed: 8161485]

Kilkenny C, Browne W, Cuthill IC, Emerson M, Altman DG, 2010. Animal research: Reporting in vivo experiments: the ARRIVE guidelines. Br. J. Pharmacol 160, 1577–1579. [PubMed: 20649561]

Kleimaier D, Goerke S, Nies C, Zaiss M, Kunz P, Bachert P, Ladd ME, Gottwald E, Schad LR, 2020. The cellular heat shock response monitored by chemical exchange saturation transfer MRI. Sci Rep 10, 11118. [PubMed: 32632120]

Kogan F, Hariharan H, Reddy R, 2013. Chemical exchange saturation transfer (CEST) Imaging: description of technique and potential clinical applications. Curr. Radiol. Rep 1, 102–114. [PubMed: 23730540]

Kogan F, Haris M, Singh A, Cai K, Debrosse C, Nanga RP, Hariharan H, Reddy R, 2014 Method for high-resolution imaging of creatine in vivo using chemical exchange saturation transfer. Magn. Reson. Med 71, 164–172. [PubMed: 23412909]

Lee VM, Trojanowski JQ, 1999. Neurodegenerative tauopathies: human disease and transgenic mouse models. Neuron 24, 507–510. [PubMed: 10595503]

Leigh R, Knutsson L, Zhou J, van Zijl PC, 2018. Imaging the physiological evolution of the ischemic penumbra in acute ischemic stroke. J. Cereb. Blood Flow Metab 38, 1500–1516. [PubMed: 28345479]

Li T, Braunstein KE, Zhang J, Lau A, Sibener L, Deeble C, Wong PC, 2016. The neuritic plaque facilitates pathological conversion of tau in an Alzheimer's disease mouse model. Nat. Commun 7, 12082. [PubMed: 27373369]

Litt L, Gonzalez-Mendez R, Severinghaus JW, Hamilton WK, Shuleshko J, Murphy-Boesch J, James TL, 1985. Cerebral intracellular changes during supercarbia: an in vivo 31P nuclear magnetic resonance study in rats. J Cereb Blood Flow Metab 5, 537–544. [PubMed: 4055925]

Lyros E, Ragoschke-Schumm A, Kostopoulos P, Sehr A, Backens M, Kalampokini S, Decker Y, Lesmeister M, Liu Y, Reith W, Fassbender K, 2020. Normal brain aging and Alzheimer's disease are associated with lower cerebral pH: an in vivo histidine (1)H-MR spectroscopy study. Neurobiol. Aging 87, 60–69. [PubMed: 31902521]

Maeda J, Zhang MR, Okauchi T, Ji B, Ono M, Hattori S, Kumata K, Iwata N, Saido TC, Trojanowski JQ, Lee VM, Staufenbiel M, Tomiyama T, Mori H, Fukumura T, Suhara T, Higuchi M, 2011. In vivo positron emission tomographic imaging of glial responses to amyloid-beta and tau pathologies in mouse models of Alzheimer's disease and related disorders. J. Neurosci 31, 4720–4730. [PubMed: 21430171]

Mandal PK, Akolkar H, Tripathi M, 2012. Mapping of hippocampal pH and neurochemicals from in vivo multi-voxel 31P study in healthy normal young male/female, mild cognitive impairment, and Alzheimer's disease. J. Alzheimers Dis 31 (Suppl 3), S75–S86. [PubMed: 22426021]

Martoft L, Stodkilde-Jorgensen H, Forslid A, Pedersen HD, Jorgensen PF, 2003. CO2 induced acute respiratory acidosis and brain tissue intracellular pH: a P-31 NMR study in swine. Lab. Anim 37, 241–248. [PubMed: 12869287]

Morales I, Guzman-Martinez L, Cerda-Troncoso C, Farias GA, Maccioni RB, 2014. Neuroinflammation in the pathogenesis of Alzheimer's disease. A rational framework for the search of novel therapeutic approaches. Front Cell Neurosci 8, 112. [PubMed: 24795567]

Mosconi L, Mistur R, Switalski R, Tsui WH, Glodzik L, Li Y, Pirraglia E, De Santi S, Reisberg B, Wisniewski T, de Leon MJ, 2009. FDG-PET changes in brain glucose metabolism from normal cognition to pathologically verified Alzheimer's disease. Eur. J. Nucl. Med. Mol. Imaging 36, 811–822.

Nishimura M, Johnson DC, Hitzig BM, Okunieff P, Kazemi H, 1989. Effects of hypercapnia on brain pHi and phosphate metabolite regulation by 31P-NMR. J Appl. Physiol 66, 2181–2188 1985. [PubMed: 2501277]

Paterson RW, Gabelle A, Lucey BP, Barthelemy NR, Leckey CA, Hirtz C, Lehmann S, Sato C, Patterson BW, West T, Yarasheski K, Rohrer JD, Wildburger NC, Schott JM, Karch CM, Wray S, Miller TM, Elbert DL, Zetterberg H, Fox NC, Bateman RJ, 2019. SILK studies - capturing the

turnover of proteins linked to neurodegenerative diseases. Nat. Rev. Neurol 15, 419–427. [PubMed: 31222062]

Petroff OA, Prichard JW, Behar KL, Alger JR, den Hollander JA, Shulman RG, 1985. Cerebral intracellular pH by 31P nuclear magnetic resonance spectroscopy. Neurology 35, 781–788. [PubMed: 4000479]

Pettegrew JW, Panchalingam K, Klunk WE, McClure RJ, Muenz LR, 1994. Alterations of cerebral metabolism in probable Alzheimer's disease: a preliminary study. Neurobiol Aging 15, 117–132. [PubMed: 8159258]

Rijpma A, van der Graaf M, Meulenbroek O, Olde Rikkert MGM, Heerschap A, 2018. Altered brain high-energy phosphate metabolism in mild Alzheimer's disease: a 3-dimensional (31)P MR spectroscopic imaging study. Neuroimage Clin 18, 254–261. [PubMed: 29876246]

Rojas JC, Boxer AL, 2016. Neurodegenerative disease in 2015: Targeting tauopathies for therapeutic translation. Nat. Rev. Neurol 12, 74–76. [PubMed: 26794651]

Saab G, Marsh GD, Casselman MA, Thompson RT, 2002. Changes in human muscle transverse relaxation following short-term creatine supplementation. Exp Physiol 87, 383–389. [PubMed: 12089606]

Saint-Aubert L, Lemoine L, Chiotis K, Leuzy A, Rodriguez-Vieitez E, Nordberg A, 2017. Tau PET imaging: present and future directions. Mol Neurodegener 12, 19. [PubMed: 28219440]

Schwartz L, Peres S, Jolicoeur M, da Veiga Moreira J, 2020. Cancer and Alzheimer's disease: intracellular pH scales the metabolic disorders. Biogerontology doi:10.1007/s10522-10020-09888-10526.

Selkoe D, Kopan R, 2003. Notch and Presenilin: regulated intramembrane proteolysis links development and degeneration. Ann. Rev. Neurosci 26, 565–597. [PubMed: 12730322]

Sugden PH, Fuller SJ, 1991. Correlations between cardiac protein synthesis rates, intracellular pH and the concentrations of creatine metabolites. Biochem. J 273, 339–346. [PubMed: 1991035]

Sui R, Chen L, Li Y, Huang J, Chan KWY, Xu X, Zijl P.C.M.v., Xu J, 2021. Whole-brain amide CEST imaging at 3T with a steady-state radial MRI acquisition. Magn. Reson. Med doi:10.1002/mrm.28770.

Thomas RC, 1976. Ionic mechanism of the H+ pump in a snail neurone. Nature 262, 54–55. [PubMed: 934324]

Thomas RC, 1977. The role of bicarbonate, chloride and sodium ions in the regulation of intracellular pH in snail neurones. J Physiol 273, 317–338. [PubMed: 23429]

Tkac I, Starcuk Z, Choi IY, Gruetter R, 1999. In vivo 1H NMR spectroscopy of rat brain at 1 ms echo time. Magn. Reson Med 41, 649–656. [PubMed: 10332839]

Tomiyama T, Matsuyama S, Iso H, Umeda T, Takuma H, Ohnishi K, Ishibashi K, Teraoka R, Sakama N, Yamashita T, Nishitsuji K, Ito K, Shimada H, Lambert MP, Klein WL, Mori H, 2010. A mouse model of amyloid beta oligomers: their contribution to synaptic alteration, abnormal tau phosphorylation, glial activation, and neuronal loss in vivo. J. Neurosci 30, 4845–4856. [PubMed: 20371804]

Trott O, Palmer AG, 2002. R 1ρ relaxation outside of the fast-exchange limit. J. Magn. Reson 154, 157–160. [PubMed: 11820837]

Tse M, Levine S, Yun C, Brant S, Pouyssegur J, Donowitz M, 1993. The mammalian Na+/H+ exchanger gene family–initial structure/function studies. J Am Soc Nephrol 4, 969–975. [PubMed: 8286718]

van Zijl PC, Yadav NN, 2011. Chemical exchange saturation transfer (CEST): what is in a name and what isn't? Magn. Reson. Med 65, 927–948. [PubMed: 21337419]

van Zijl PCM, Lam WW, Xu J, Knutsson L, Stanisz GJ, 2018. Magnetization transfer contrast and chemical exchange saturation transfer MRI. Features and analysis of the field-dependent saturation spectrum. Neuroimage 168, 222–241. [PubMed: 28435103]

Vermathen P, Capizzano AA, Maudsley AA, 2000. Administration and (1)H MRS detection of histidine in human brain: application to in vivo pH measurement. Magn. Reson Med 43, 665–675. [PubMed: 10800031]

Vinogradov E, Sherry AD, Lenkinski RE, 2013. CEST: from basic principles to applications, challenges and opportunities. J. Magn. Reson 229, 155–172. [PubMed: 23273841]

Wang R, Chen P, Shen Z, Lin G, Xiao G, Dai Z, Zhang B, Chen Y, Lai L, Zong X, Li Y, Tang Y, Wu R, 2019. Brain amide proton transfer imaging of rat with Alzheimer's disease using saturation with frequency alternating rf irradiation method. Front Aging Neurosci. 11, 217. [PubMed: 31507405]

Yoshiyama Y, Higuchi M, Zhang B, Huang SM, Iwata N, Saido TC, Maeda J, Suhara T, Trojanowski JQ, Lee VM, 2007. Synapse loss and microglial activation precede tangles in a P301S tauopathy mouse model. Neuron 53, 337–351. [PubMed: 17270732]

Zaiss M, Bachert P, 2013a. Chemical exchange saturation transfer (CEST) and MR Z-spectroscopy in vivo: a review of theoretical approaches and methods. Phys. Med. Biol 58, R221. [PubMed: 24201125]

Zaiss M, Bachert P, 2013b. Exchange-dependent relaxation in the rotating frame for slow and intermediate exchange – modeling off-resonant spin-lock and chemical exchange saturation transfer. NMR Biomed. 26, 507–518. [PubMed: 23281186]

Zaiss M, Zu Z, Xu J, Schuenke P, Gochberg DF, Gore JC, Ladd ME, Bachert P, 2015 A combined analytical solution for chemical exchange saturation transfer and semi-solid magnetization transfer. NMR Biomed. 28, 217–230. [PubMed: 25504828]

Zhang XY, Xie J, Wang F, Lin EC, Xu J, Gochberg DF, Gore JC, Zu Z, 2017. Assignment of the molecular origins of CEST signals at 2 ppm in rat brain. Magn Reson Med. 78, 881–887. [PubMed: 28653349]

Zhang Z, Zhang C, Yao J, Chen X, Gao F, Jiang S, Chen W, Zhou J, Wang G, 2020. Protein-based amide proton transfer-weighted MR imaging of amnestic mild cognitive impairment. Neuroimage Clin. 25, 102153. [PubMed: 31901792]

Zhou IY, Lu D, Ji Y, Wu L, Wang E, Cheung JS, Zhang XA, Sun PZ, 2019. Determination of multipool contributions to endogenous amide proton transfer effects in global ischemia with high spectral resolution in vivo chemical exchange saturation transfer MRI. Magn Reson Med. 81, 645–652. [PubMed: 30058148]

Zhou J, Payen JF, Wilson DA, Traystman RJ, van Zijl PC, 2003. Using the amide proton signals of intracellular proteins and peptides to detect pH effects in MRI. Nat. Med 9, 1085–1090. [PubMed: 12872167]

Zhou JY, van Zijl PCM, 2006. Chemical exchange saturation transfer imaging and spectroscopy. Prog. Nucl. Magn. Reson. Spectrosc 48, 109–136.

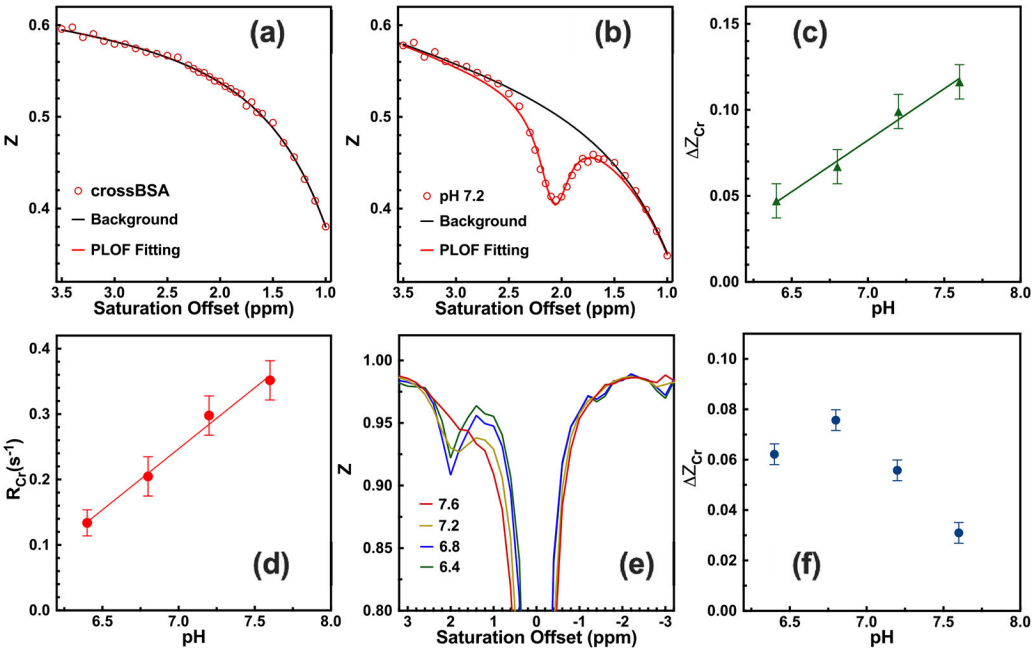

Fig 1.

Typical phantom CrCEST Z-spectra of (a) 15% CrossBSA only and (b) 50mM Cr with 15% CrossBSA (pH 7.2), acquired using a B_1 of 2 μT and a saturation length of 1 s. Solid lines are the fitted background and the CEST peaks with the PLOF method. Identical PLOF fitting parameters were used for the fitting range and peak range in (a) and (b). In the fitting, the measured water T_1 of 2.8 s^{-1} was used. (c) pH dependence of the Cr CEST signal. The solid line stands for the linear fit (R^2 = 0.99). (d) pH-dependence of the R_{Cr} signal. The solid line stands for the linear fit (R^2 = 0.99). (e) Typical phantom CrCEST Z-spectra of 10 mM Cr solutions with pH = 7.6, 7.2, 6.8 and 6.4. (f) The CrCEST signal as a function of pH value for the Cr solutions. The CrCEST was extracted by subtracting the Z-values at ±2 ppm.

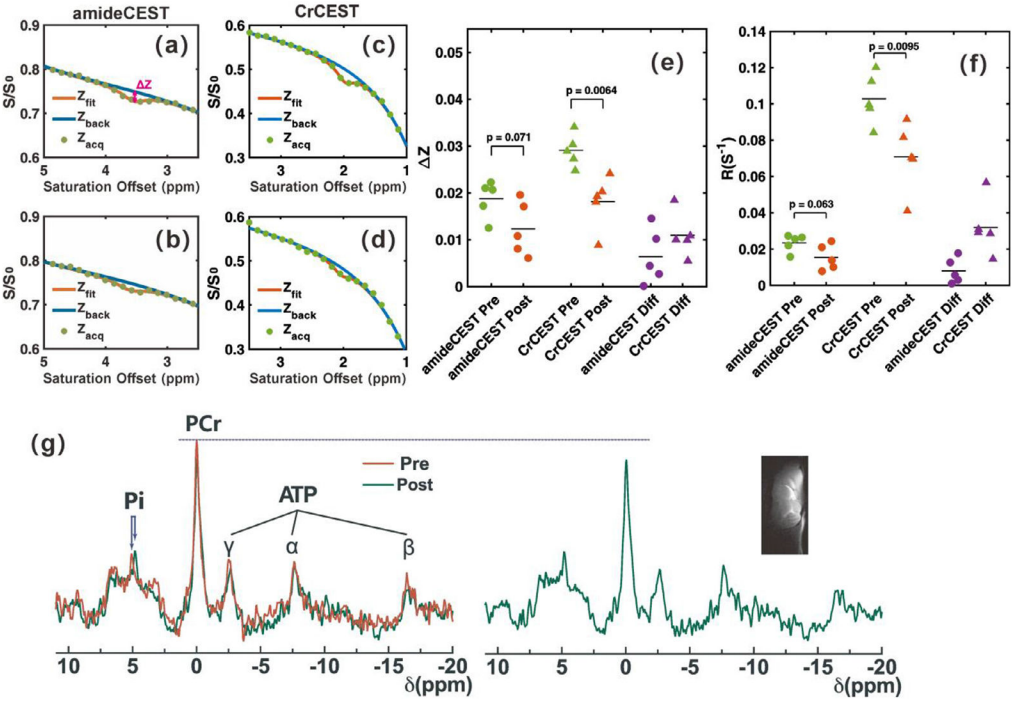

Fig 2.

Sensitivity of amideCEST and CrCEST MRI for detecting pH changes in mouse brain during CO_2 inhalation. Representative Z-spectra for the amideCEST experiments (a) pre-CO_2 and (b) during CO_2 inhalation for the cortex region in Fig. 3a. Representative Z-spectra of CrCEST experiment (c) pre-CO_2 and (d) during CO_2 inhalation for this cortex region. Solid lines are the background fitted using the PLOF method. (e) Scatter plots showing the difference for amideCEST and CrCEST experiments obtained by PLOF (n= 5) and the corresponding changes in the apparent relaxation rate in the rotating frame of amide (R_{amide}) and creatine (R_{Cr}) protons (f). (g) Averaged ^{31}P spectra (n=4) for the WT mice pre (red) and during (green) CO_2 inhalation. The shift of the inorganic phosphate (Pi) due to the pH change is indicated. The PCr peaks clearly showed signal reduction and broadening after CO_2 inhalation, while the adenosine triphosphate concentration showed a negligible change. A typical T_2w image of the mouse brain is shown to judge the coverage of the ^{31}P/^{1}H surface coil.

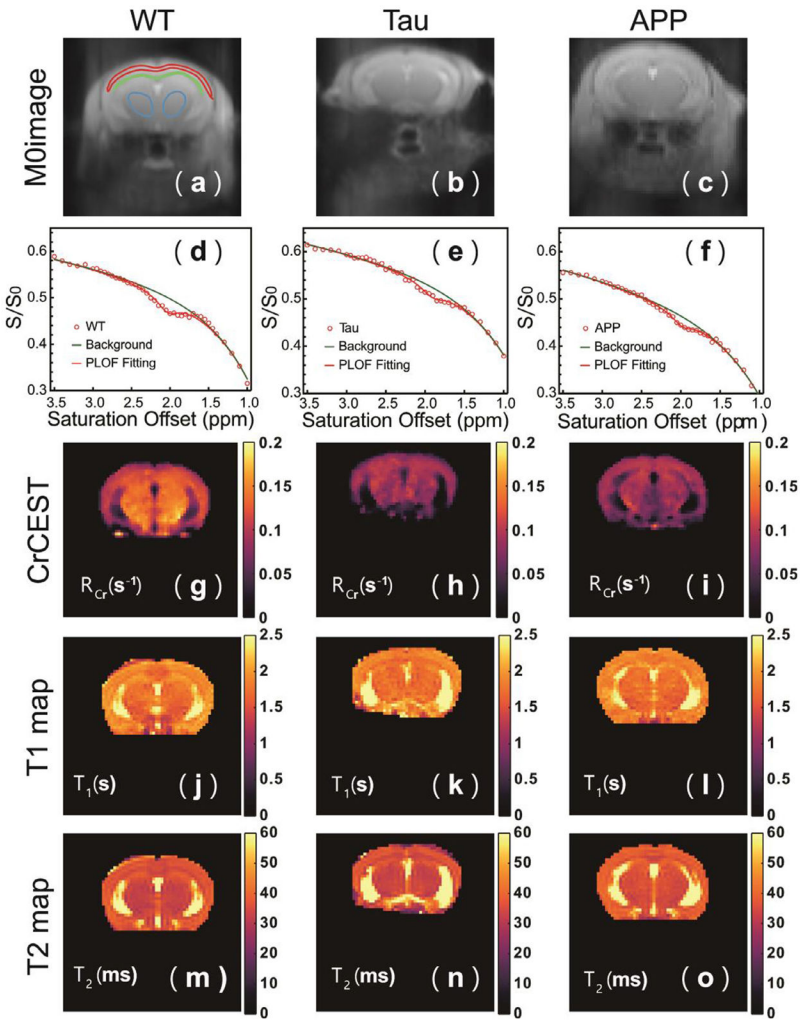

Fig 3.

Typical S_0 images (a, b, c), cortical CrCEST Z-spectra (d, e, f), CrCEST maps (g, h, i), T_1 maps (j, k, l), and T_2 maps (m,n,o) for WT (a, d, g, j, m), Tau (b, e, h, k, n), and APP (c, f, i, l, o) mice. Both CrCEST Z-spectra and CrCEST maps (R_{Cr}) of Tau and APP mice show a clear signal reduction compared to WT mice, while the T_1 and T_2 maps closely resemble each other among the three types of mice. The ROIs used to extract regional values are indicated in (a). The Z-spectra in d, e and f are from the cortical ROI in (a).

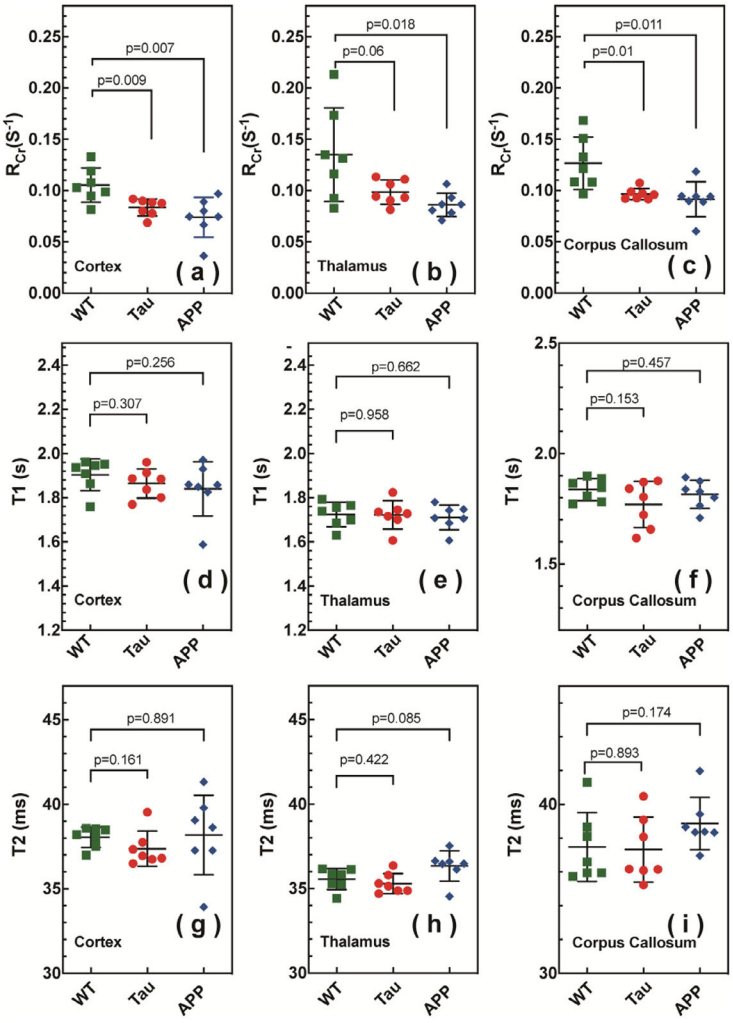

Fig 4.

The CrCEST apparent relaxation rates in the rotating frame (R_{Cr}) for cortex (a), thalamus (b), and corpus callosum (c) in WT (green square), Tau (red circle), and APP (blue diamond) mice. The CrCEST effect of Tau and APP mice shows a clear reduction compared to WT mice. The T_1 values for cortex (d), thalamus (e), and corpus callosum (f) in WT (green square), Tau (red circle) and APP (blue diamond) mice are not significantly different. The T_2 values for cortex (g), thalamus (h), and corpus callosum (i) in WT (green square), Tau (red circle) and APP (blue diamond) mice are not significantly different.

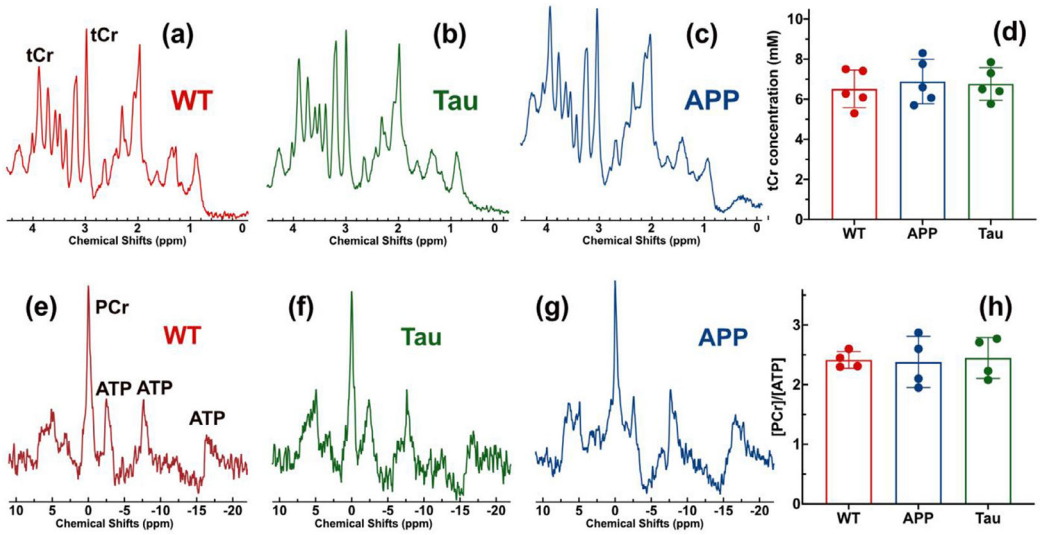

Fig 5.

Typical *in vivo* proton MRS spectra for (a) WT, (b) Tau and (c) APP mouse brains. (d) The tCr concentrations extracted from the proton spectrum through fitting with LCModel. There are no clear tCr concentration differences between the three types of mice. The averaged ^{31}P MRS spectra (n=4) of (e) WT, (f) Tau, and (g) APP mouse brains. The coil coverage was identical to that in Fig. 1g. (e) The PCr to ATP concentration ratios (n = 4) extracted from the 31P MRS.

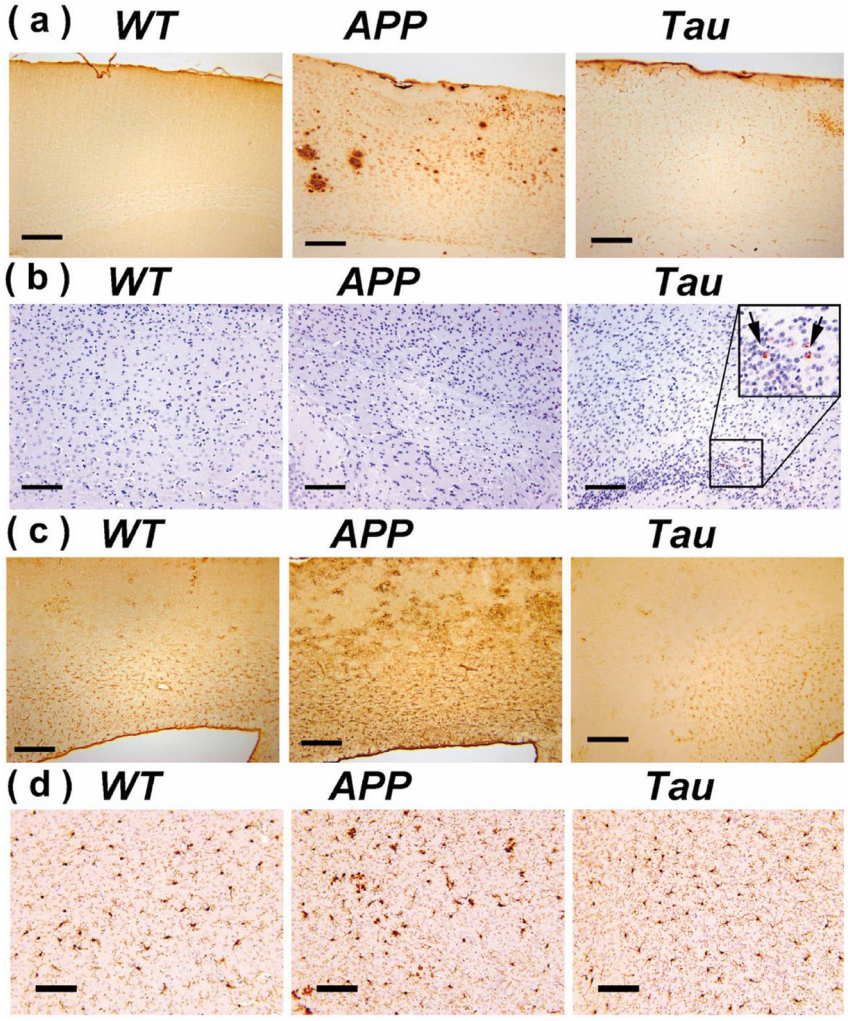

Fig 6.

Brain sections of WT, APP and Tau mice stained by antibodies specific to Aβ (6E10) (a), phosphorylated tau: Tau-pS422 (b), reactive astrocytes (GFAP) (c), and microglia (IBA1) (d). Scale bars are 200 μm in (a-c) and 100 μm in (d).

Table 1

Averaged values of R_{Cr}, T_1, and T_2 for the WT, Tau and APP mice ($n = 7$) for three different brain regions: cortex (cx), thalamus (th) and corpus callosum (cc). The error indicates the standard derivation among seven mice in each group.

		R_{Cr} (s^{-1})	T_1 (s)	T_2 (ms)
WT	cx	0.105±0.017	1.90±0.07	38.05±0.60
	th	0.135±0.046	1.72±0.06	35.56±0.60
	cc	0.127±0.026	1.84±0.05	37.47±2.04
Tau	cx	0.084±0.083	1.86±0.07	37.37±1.04
	th	0.099±0.012	1.72±0.06	35.29±0.59
	cc	0.097±0.006	1.77±0.10	36.33±1.92
APP	cx	0.074±0.019	1.84±0.12	38.18±2.35
	th	0.086±0.011	1.71±0.06	36.34±0.90
	cc	0.092±0.017	1.82±0.06	38.87±1.55